Korean J. Chem. Eng., 38(4), 704-715 (2021)
DOI: 10.1007/s11814-020-0737-5

pISSN: 0256-1115
eISSN: 1975-7220

Effect of alumina nanoparticle shape in a triangular porous array of heated periodic pin-fins

Mohd Asif and Amit Kumar Dhiman†

Chemical Engineering Department, Indian Institute of Technology Roorkee, Roorkee 247 667, Uttarakhand, India

(*Received 1 October 2020 • Revised 1 December 2020 • Accepted 23 December 2020*)

Abstract−Forced convective flow of alumina-water nanofluid with different shapes of nanoparticles through pin-fins of circular cross-section aligned in an equilateral triangular array was analyzed using finite volume methodology. The effect of the shape of alumina nanoparticles on heat transfer across the periodic equilateral triangular array has never been studied in the past. Four different shapes of nanoparticles were considered: spherical, cylindrical, bricks, and platelets. Using non-spherical (cylindrical, bricks, and platelets) nanoparticles resulted in a thinning thermal boundary layer, which resulted in a significant enhancement in heat transfer rates across the array. The mean Nusselt number was augmented by 22% when platelet shaped nanoparticles were utilized in place of spherical shaped nanoparticles. Likewise, the mean Nusselt number was augmented by 17% when cylindrical nanoparticles were used, in place of spherical nanoparticles, at the highest values of other parameters. The increment in effective viscosity of the nanofluid was the highest for platelet-shaped nanoparticles, which resulted in a greater pressure drop compared to other shapes of nanoparticles such as cylindrical, bricks, and spherical for all values of particle concentration. The results in the present article are validated extensively with accessible experimental and numerical studies.

Keywords: Triangular Array, Nanoparticle Shape, Pin-fins, Pumping Power and Pressure Drop

INTRODUCTION

Periodic arrays of pin-fins with a convective flow generally occur in numerous crucial engineering processes such as food processing, compact heat-exchange systems, nuclear reactors, polymer processing, and filtration [1-5]. The utilization of pin-fin heat exchangers/sinks is becoming prevalent in various thermal engineering processes due to their high heat transfer coefficients resulting from the disruption of the boundary layer caused by mixing effects and, besides, high surface area to volume ratio [6,7]. A vital application involving pin-fin arrays is the thermal management of electronic components such as transistors, printing circuit boards (PCB), and an integrated set of electronic circuits [8,9]. When an external energy source such as a pump or a blower is used, forced convection is said to occur across multiple heated electronic components in PCB or an integrated set of electronic circuits imitating a pin-fin heat exchanger.

At present, the focus of research is on analyzing the hydro-thermal performance of such heat-exchange systems for better energy management. For this purpose, the utilization of nanofluids, which are the suspension of nano-sized particles in base fluids, instead of conventional fluids such as water, oils, and ethylene as an energy carrier fluid, is gaining popularity due to their enhanced thermal conductivity. In the present work, alumina (Al_2O_3)-water nanofluid is considered as a cooling fluid flowing through an equilateral triangular array of pin-fins. The equilateral triangular array of cylinders (pin-fins) has high heat transfer coefficients compared to a square array of cylinders and is preferred when the pressure drop is steep [3]. Also, the efficiency of the triangular array of cylinders is higher as more tubes can be accommodated within it. Erstwhile studies involving pin-fin heat exchangers mainly focus on various geometrical parameters such as fin shape and size, the arrangement of fins, porosity, and type of cooling fluids. Nevertheless, the effect of the shape of nanoparticles in a nanofluid on the hydro-thermal behavior of a pin-fin heat exchanger is not being analyzed in the scientific literature.

Researchers have examined the convective heat transfer across periodic array geometry in heat exchange-systems to find ways to improve the heat transfer rates. Ram et al. [10] analyzed the cross flow in an inline square array of periodic cylinders and postulated mathematical equations for drag and average Nusselt numbers. However, Asif and Dhiman [11] analyzed the fluid flow through the periodic triangular array of cylinders. The flow and thermal characteristics are depicted thoroughly with the alteration of average drag coefficient, local and average Nusselt numbers against Re, Pr, and porosity. Wung and Chen [12] and Chen and Wung [13] employed an inline square array and a staggering array of cylinders to analyze the flow and heat transfer across the respective arrays, and the experimental outcome of Zukauskas et al. [14] for tube banks concurred thoroughly with them [12,13]. A critical numerical study related to periodic arrays (triangular and square) of cylinders is reported by Martin et al. [3]. The study stipulates the power-law correlations for frictional losses and Nusselt number for available area fractions more significant than 0.8.

Recently, the use of nanofluids as an energy carrier fluid has taken the lead in heat-exchange systems. More and more research-

†To whom correspondence should be addressed.
E-mail: amit.dhiman@ch.iitr.ac.in, dhimuamit@rediffmail.com

ers are using nanofluids [15-24] for the sole reason of their improved thermal conductivity and better stability. Asif et al. [23] analyzed the forced convective flow of alumina-water nanofluid across an inline and a staggered array of cylinders in a heat exchanger. Their study [23] revealed that the mean Nusselt number is increased by 20% in the inline array and by 60% in the staggered array when nanoparticle diameter is reduced from 50 nm to 10 nm. Sheikholeslami and Farshad [24] examined the turbulent nanoparticle transport inside a tube with quad-channel tapes involving solar radiation. They demonstrated that better mixing happens with such devices and the rate of cooling is augmented. Selvakumar and Dhinakaran [25] studied forced convective heat transfer using nanofluids past a circular cylinder using single and multiphase approaches. They calculated effective thermal conductivity and viscosity using correlations that incorporate the effects of nanoparticle diameter and temperature. Lavasani and Bayat [26] compared forced convective heat transfer and pressure drop between cam-shaped and circular tube banks using alumina-water nanofluid for inline and staggered arrangements. They [26] used the Brinkman equation [27] and the Maxwell-Garnett [28] model for calculating effective viscosity and thermal conductivity. They [26] deduced that cam-shaped tubes have higher heat transfer rates in comparison to circular tubes. Also, high thermal efficiency is observed in the staggered arrangement for both kinds of tube bundles.

The majority of the studies involving nanofluids do not consider the shape of the nanoparticle. In contrast, only a few studies are available that inquire about the effect of the shape of nanoparticles in various systems. Nguyen et al. [29] studied the change in thermal characteristics for the flow of different shaped CuO nanoparticle-water nanofluid across a wavy-channel with obstacles and developed mathematical correlations for mean Nusselt number. Ellahi et al. [30] analyzed the effect of the shape of the nanosize particle in CuO-water nanofluids flowing inside an inverted cone. They [30] showed that entropy of the system increased when platelet-shaped nanoparticles were employed. Vanakhi et al. [31] studied the influence of different shapes of SiO_2 nanoparticles. Their results demonstrated an increment in the mean Nusselt number of the channel when platelet-shaped SiO_2 nanoparticles were used in place of spherical ones.

The aforesaid brief literature survey provides the evidence that

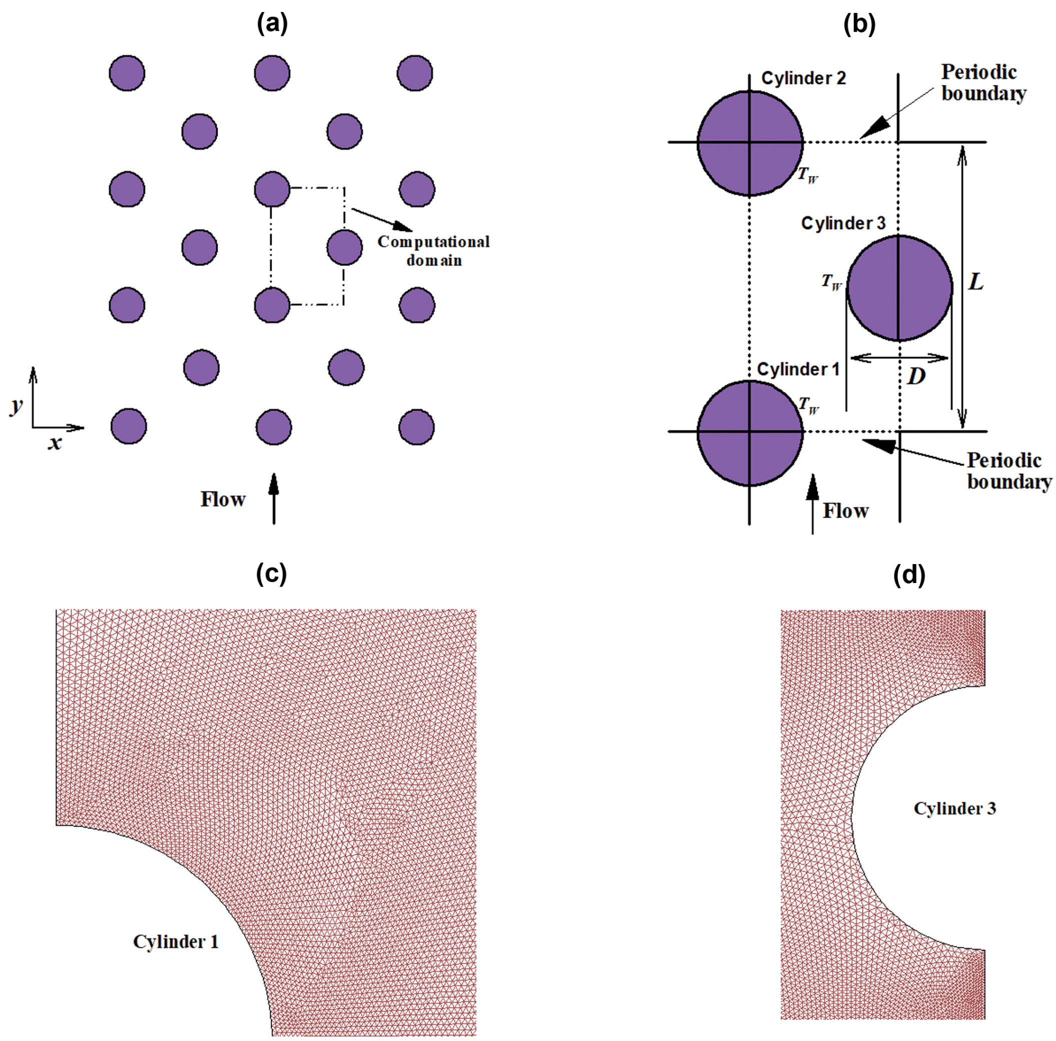

Fig. 1. (a) Flow schematic, (b) computational domain, (c) mesh around cylinder 1, and (d) mesh around cylinder 3 in a pin-fin type heat-exchanger.

the researchers have analyzed the flow of nanofluids across arrays of cylinders. Still, no studies are available that portray the alumina nanoparticle-shape effect on hydro-thermal behavior through periodic arrays of pin-fins arranged in an equilateral triangular arrangement in a heat exchanger. Therefore, it is important to fill this research gap. Hence, the present numerical study was performed to quantify the various control parameters across a periodic triangular array of pin-fins for the forced convective flow of alumina-water nanofluids having differently shaped nanoparticles. The best-suited shape of nanoparticles for heat transfer enhancement across the equilateral triangular array of circular cross-section pin-fins has been proposed via the present analysis. The finite volume method was employed for the current computational framework, and the effect of Re, particle concentration and shape of alumina nanoparticle on flow and thermal characteristics were determined.

PROBLEM STATEMENT

Schematically, Fig. 1(a) depicts the convective flow of alumina-water nanofluid through heated pin-fins in a heat exchanger. The cylinders are arranged so that if the three pin-fins are connected in the array, they form an equilateral triangle. The simulations are carried out by simplifying a fundamental unit cell, as shown in Fig. 1(b), which repeats itself in space at transverse distance L, making the inlet and outlet a periodic boundary. The cylinder's diameter is denoted as D, and the center to center distance between the cylinders is L. The position of the cylinders in the triangular array is determined by using porosity ε relation with spacing ratio L/D [3] as:

$$\varepsilon=1-\frac{\Pi}{2\sqrt{3}}\left(\frac{L}{D}\right)^{-2} \tag{1}$$

The laminar flow is considered to be in the y-direction, as depicted in Fig. 1. The various physical parameters used in the present analysis are Re, which is varied in the range 10-200, nanoparticle concentration ϕ in the range 0.01-0.04, and four distinct shapes of Al_2O_3 nanoparticles: spherical, bricks, cylindrical, and platelets. Our previous studies have already analyzed the effect of porosity on convective heat transfer across periodic arrays [10,11,32]. Hence, the porosity of the array of cylinders is fixed at 0.8, which corresponds to the ratio of the transverse and longitudinal distance between the cylinders as less than two and a common occurrence in industrial operations [33].

MATHEMATICAL MODEL AND BOUNDARY CONDITIONS

To solve the present problem the assumptions are made while writing mathematical expressions for the conservation of mass, momentum, and energy (Eqs. (2)-(5)): Flow is steady, laminar, and two-dimensional; the fluid is incompressible, Newtonian, with constant thermophysical properties; the end effects are negligible and negligible viscous dissipation.

$$\frac{\partial \hat{u}}{\partial \hat{x}}+\frac{\partial \hat{v}}{\partial \hat{y}}=0 \tag{2}$$

$$\hat{u}\frac{\partial \hat{u}}{\partial \hat{x}}+\hat{v}\frac{\partial \hat{u}}{\partial \hat{y}}=-\frac{\rho_f}{\rho_{nf}}\frac{\partial \hat{p}}{\partial \hat{x}}+\frac{\vartheta_{nf}}{\vartheta_f}\mathrm{Pr}\left(\frac{\partial^2 \hat{u}}{\partial \hat{x}^2}+\frac{\partial^2 \hat{u}}{\partial \hat{y}^2}\right) \tag{3}$$

$$\hat{u}\frac{\partial \hat{v}}{\partial \hat{x}}+\hat{v}\frac{\partial \hat{v}}{\partial \hat{y}}=-\frac{\rho_f}{\rho_{nf}}\frac{\partial \hat{p}}{\partial \hat{y}}+\frac{\vartheta_{nf}}{\vartheta_f}\mathrm{Pr}\left(\frac{\partial^2 \hat{v}}{\partial \hat{x}^2}+\frac{\partial^2 \hat{v}}{\partial \hat{y}^2}\right) \tag{4}$$

$$\hat{u}\frac{\partial \hat{T}}{\partial \hat{x}}+\hat{v}\frac{\partial \hat{T}}{\partial \hat{y}}=\frac{\alpha_{nf}}{\alpha_f}\left(\frac{\partial^2 \hat{T}}{\partial \hat{x}^2}+\frac{\partial^2 \hat{T}}{\partial \hat{y}^2}\right) \tag{5}$$

where $\vartheta_{nf}=\frac{\mu_{nf}}{\rho_{nf}}$, $\alpha_{nf}=\frac{k_{nf}}{(\rho c_p)_{nf}}$ and $\mathrm{Pr}=\left(\frac{\mu c_p}{k}\right)_f$. The equations mentioned above are made non-dimensional by using diameter D as the length scale for x and y coordinates and α_f/D as the velocity scale for obtaining non-dimensional velocity $\hat{u}$ [$=uD/\alpha_f$] & $\hat{v}$ [$=vD/\alpha_f$]. $\hat{T}$ is the dimensionless temperature being defined as $\hat{T}=(T-T_\infty)/(T_w-T_\infty)$, where T is dimensional temperature. A scaling factor $\rho_f\alpha_f^2/D^2$ is used for getting non-dimensional pressure $\hat{p}$ [$=pD^2/\rho_f\alpha_f^2$]. The subscripts nf and f stand for nanofluid and fluid, respectively.

The non-dimensional governing Eqs. (2)-(5) are solved by employing the ensuing boundary conditions: At the inlet, uniform flow in the *y*-direction is assumed. No-slip velocity condition and constant wall temperature are prescribed at cylindrical walls. The periodic boundary condition is applied at the inlet and outlet, which in mathematical terms means:

$$\hat{u}_{in}=\hat{u}_{out}=0,\ \hat{v}_{in}=\hat{v}_{out}\ \text{and}\ \hat{T}_{in}=\hat{T}_{out} \tag{6}$$

subscripts '*in*' and '*out*' represent the inlet and outlet periodic boundaries, respectively.

The surfaces which are in contact with the pin-fins vertically (symmetric plane) have no flow in the longitudinal direction, and the normal gradients of velocity as well as temperature are negligible.

Local Nusselt number (Nu_θ) is utilized to measure the heat transfer rates from the pin-fins and represented as

$$Nu_\theta=\frac{h_{nf}D}{k_{nf}}=-\left.\frac{\partial \hat{T}}{\partial \hat{r}}\right|_{1/2} \tag{7}$$

where h is the coefficient of heat transfer, r is the cylinder's surface, and defined as $\hat{r}=\sqrt{\hat{x}^2+\hat{y}^2}=1/2$. On integrating Nu_θ over the cylindrical surface, the mean Nusselt number Nu_m of each cylinder is obtained as

$$Nu_m=\frac{1}{\pi}\int_0^\pi Nu_\theta d\theta \tag{8}$$

The pressure drop ΔP across the array is defined as

$$\Delta P=P_{in}-P_{out} \tag{9}$$

where P_{in} and P_{out} represent the inlet and outlet pressures, respectively.

Furthermore, pumping power (PP) is also calculated using pressure drop and is defined as

$$PP=\Delta P V_f \tag{10}$$

where V_f represents the volumetric flow rate across the array.

The individual thermo-physical properties of alumina and water are presented in Table 1. The effective density ρ_{nf} and heat capacity $c_{p,nf}$ of the nanofluid are calculated as [34]:

Table 1. Thermo-physical properties of base fluid and nanoparticles [25]

Thermo-physical property	Water	Alumina (Al_2O_3)
Thermal conductivity (W/m·K)	0.6	40
Dynamic viscosity (kg/m·s)	0.001	-
Density (kg/m^3)	997	3,970
Heat capacitance (J/kg·K)	4,179	765

$$\rho_{nf}=(1-\phi)\rho_f+\phi\rho_p \tag{11}$$

$$(\rho c_p)_{nf}=(1-\phi)(\rho c_p)_f+\phi(\rho c_p)_p \tag{12}$$

where ϕ is the nanoparticle concentration, and subscript 'p' stands for nanoparticles.

The effective thermal conductivity and effective viscosity of the nanofluid having spherical nanoparticles are estimated as [35]:

$$\frac{k_{nf}}{k_f}=1+4.4\mathrm{Re}_p^{0.4}\mathrm{Pr}_f^{0.66}\left(\frac{T}{T_{fr}}\right)^{10}\left(\frac{k_p}{k_f}\right)^{0.03}\phi^{0.66} \tag{13}$$

$$\frac{\mu_f}{\mu_{nf}}=1-34.87\left(\frac{d_p}{d_f}\right)^{-0.3}\phi^{1.03} \tag{14}$$

where Re_p is the nanoparticle Reynolds number because of Brownian motion.

$$\mathrm{Re}_p=\frac{2\rho_f K_B T}{\pi\mu_f^2 d_p} \tag{15}$$

where Pr_f is Prandtl number of base fluid; T and T_{fr} are the temperatures of the nanofluid and freezing point of base fluid (water), respectively; K_B is the Boltzmann constant (1.38×10^{-23}); d_p is the diameter of spherical nanoparticle, which is fixed at 25 nm and d_f is the diameter of the base fluid molecule which is given as

$$d_f=0.1\left(\frac{6M}{N\pi\rho_f}\right)^{1/3} \tag{16}$$

where N is the Avogadro number, and M is the molecular weight of water.

The effective thermal conductivity and effective viscosity of the nanofluid with non-spherical shaped nanoparticles are calculated as [36]:

$$\frac{k_{nf}}{k_f}=1+\sigma_k\phi \tag{17}$$

$$\frac{\mu_{nf}}{\mu_f}=1+\eta_1\phi+\eta_2\phi^2 \tag{18}$$

where σ_k is the thermal conductivity enhancement coefficient and η_1 and η_2 are viscosity enhancement coefficients for non-spherical particles. The values of these coefficients for varied shapes are given in Table 2 along with the aspect ratios of different shapes of nanoparticles. The characterization of different shapes of nanoparticles is shown in Fig. 2.

The present analysis is a single-phase approach for modeling nanofluids, which considers the mixture of nanosized particles and base fluid as a single homogeneous phase. Both nanoparticles and base fluid are assumed to be in thermal equilibrium without any slip between their molecules. In a single-phase approach, the effective properties of the nanofluid are calculated for substitution in the governing equations. By putting the values of various coefficients given in Table 2 in Eqs. (17) and (18), effective thermal conductivity and effective viscosity of nanofluid are calculated for different nanoparticle shapes. These calculated values are then used in the governing Eqs. (3)-(5) to calculate various flow and heat transfer parameters.

Table 2. Thermophysical properties enhancement coefficients [36]

Nanoparticle shape	σ_k	η_1	η_2	Aspect ratio
Bricks	3.37	1.9	471.4	1 : 1 : 1
Cylindrical	3.95	13.5	904.4	1 : 8
Platelets	2.61	37.1	612.6	1 : 1/8

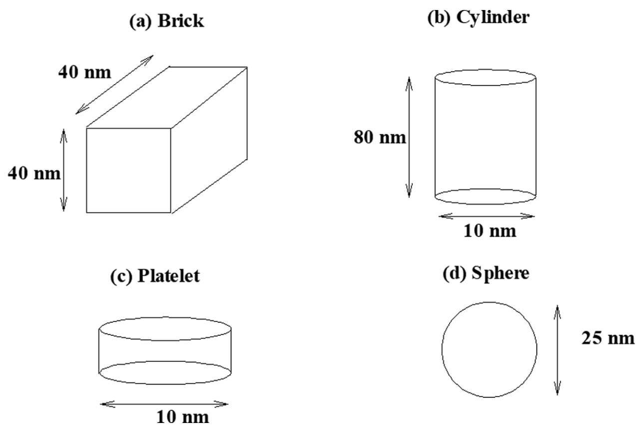

Fig. 2. Characterization of different shapes of nanoparticles [35,36].

MESH SENSITIVITY AND VALIDATION

The mesh sensitivity is examined by generating five unstructured grids using ANSYS design modeler. The five grids are classed as coarser, coarse, fine, very fine, and ultra-fine, as depicted in Table 3. The disparity between the mean Nusselt number obtained using coarser and ultra-fine grids is 0.14%, proving that the grid is independent of its size. Hence, the fine grid is used in the present analysis considering the computational expenses. The magnified grid around the cylinders is shown in Fig. 1(c) and 1(d).

To verify the reliability of the present computational model, the results are validated with the available experimental and numerical data in the literature [3,14,25,37]. Zukauskas [14] proposed the following correlation for the average Nusselt number of a cylinder

Table 3. Grid sensitivity analysis

Grid	Number of cells	Average Nusselt number
Coarser	17,276	4.8217
Coarse	21,840	4.8198
Fine	24,094	4.8173
Very fine	32,998	4.8169
Ultrafine	47,094	4.8148

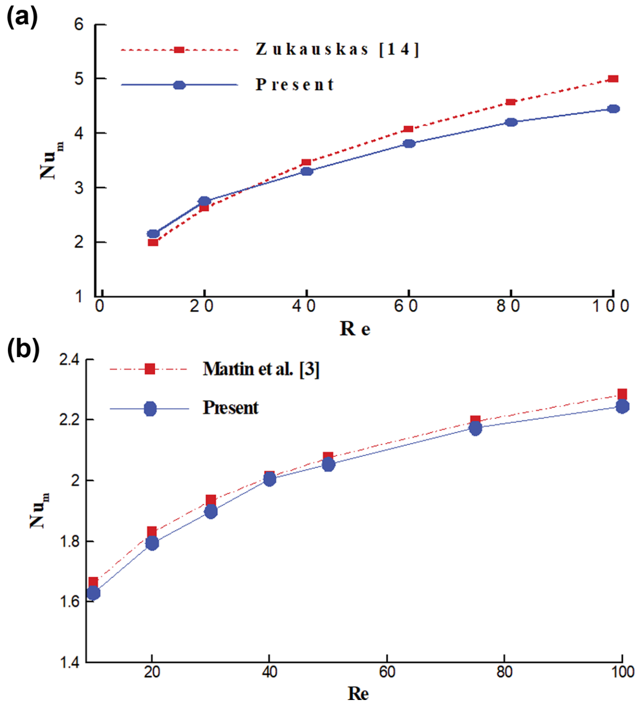

Fig. 3. Comparison of present results with (a) experimental results of Zukauskas [14] and (b) the numerical work of Martin et al. [3].

in a staggered array of cylinders:

$$Nu_m = nRe^{0.4} Pr_f^{0.36} \left(\frac{Pr_f}{Pr_w}\right)^{0.25} \tag{19}$$

Fig. 3(a) shows that the heat transfer outcomes acquired in the present study, with air as the working fluid, and the experimental results of Zukauskas [14] estimated from Eq. (19) are matching closely with each other. In addition, the mean Nusselt number (Nu_m) obtained in the present study is analyzed in contrast to the computational results of Martin et al. [3] (Fig. 3(b)). For that purpose, computations are performed at ε=0.99 and air is utilized as a working fluid. The results of both studies are close to each other.

Another essential formulation for the flow across a heated circular cylinder is given by Lange et al. [37] for Re≤200 for the flow of air as:

$$Nu_m = 0.082Re^{0.5} + 0.734Re^{y} \tag{20}$$

$$y = 0.05 + 0.226Re^{0.085} \tag{21}$$

The present values of average Nusselt number at porosity, ε=0.99 when each cylinder behaves as an individual cylinder [11] are matching closely with the results of Lange et al. [37], which are estimated by Eqs. (20) and (21) (Fig. 4).

The present method is also verified by considering the flow of alumina-water nanofluid around a single-cylinder using the correlations [35] employed in the present study for spherical particles, and the outcomes are similar to the results available in the literature [25], as illustrated in Table 4. Apart from heat transfer results, validation is also comprehended for the flow results. The pressure drop obtained in the present work using air as working fluid is non-dimensionalized in accordance with Martin et al. [3], and the resulting dimensionless pressure drop is in close resemblance with the

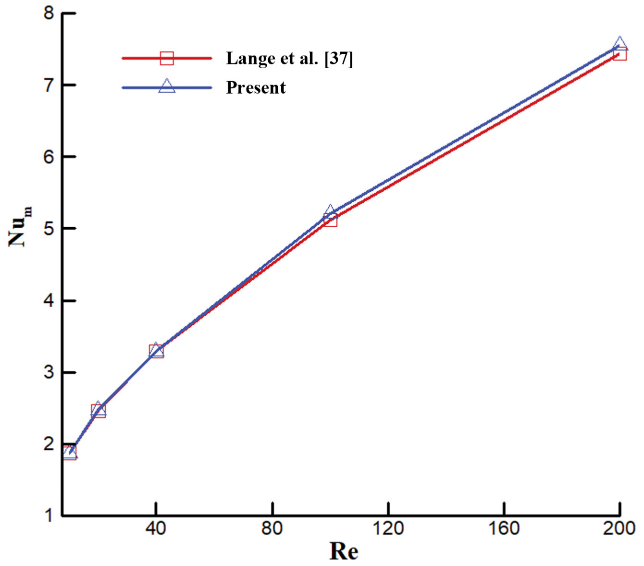

Fig. 4. Comparison of average Nusselt number on a cylinder's surface in the present study with the literature [37].

Table 4. Nusselt number comparison of the present study with the literature [25] using Corcione's [35] correlation at Re=40

ϕ	d_p (nm)	Selvakumar and Dhinakaran [25]	Present	Deviation (%)
0.02	10	7.0798	7.0220	0.82
	50	6.8987	6.8834	0.22
0.05	10	8.2907	8.3257	0.42
	50	7.2541	7.2996	0.62

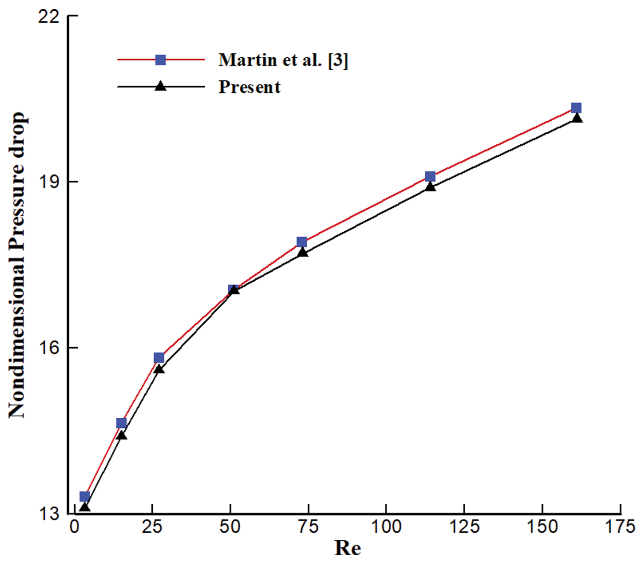

Fig. 5. Comparison of pressure drop obtained in the present study with the literature [3].

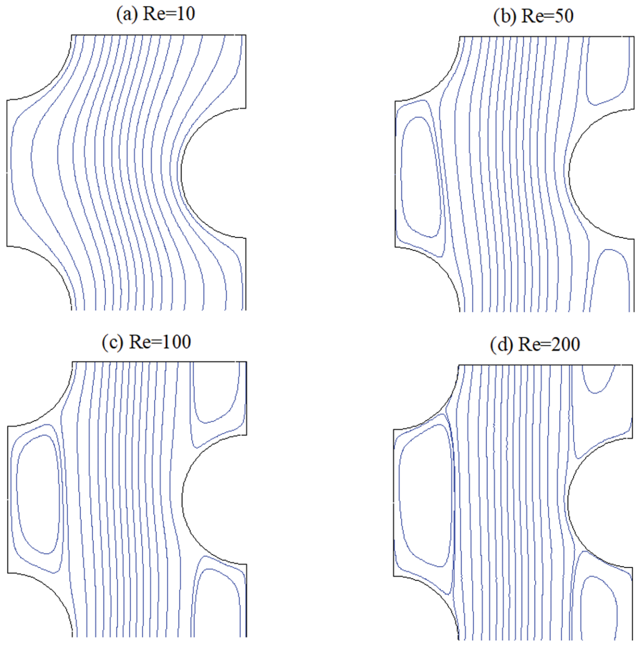

Fig. 6. Streamlines across an array of cylinders for spherical shaped nanoparticles at different Re and ϕ=0.04.

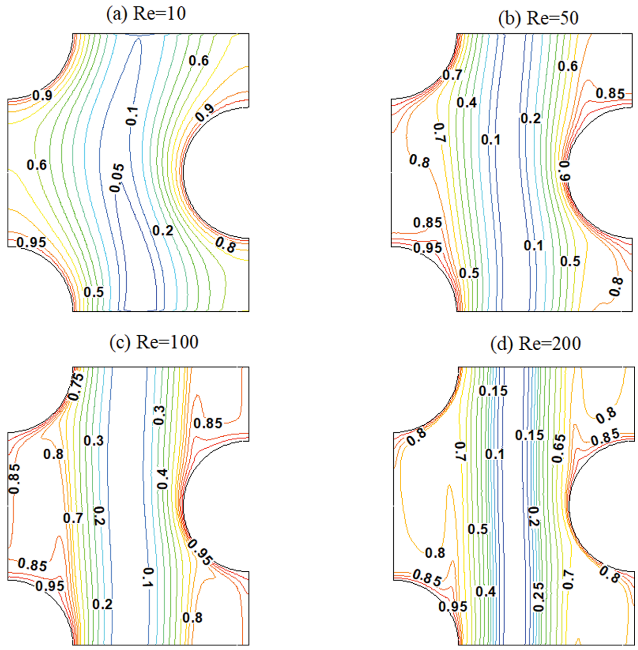

Fig. 7. Isotherms across an array of cylinders for spherical shaped nanoparticles at different Re.

dimensionless pressure drop reported in the literature [3] (Fig. 5).

RESULTS AND DISCUSSION

The computations were carried out for Re in the range 10-200, ϕ in the range 0.01-0.04, and four shapes of nanoparticles, i.e., spherical, bricks, cylindrical, and platelets at a fixed value of ε=0.8. The outcomes were then demonstrated by streamlines, isotherms, plots of local Nusselt numbers, mean Nusselt number, pressure drop, and pumping power of the triangular array of pin-fins. Mathematical correlations were derived to calculate the mean Nusselt number of the triangular array for different shapes of alumina nanoparticles under the present conditions.

1. Streamlines and Isotherms

In the present investigation, the fluid inertia has a profound effect on the hydro-thermal behavior across the triangular array of pin-fins for the flow of alumina-based nanofluids. Fig. 6 shows the streamlines across the triangular array at different Re for the flow of alumina-water nanofluid having spherical alumina particles. The nanofluid recirculation zone develops at the aft of the cylinders at Re=50, which grows in size as the inertial forces increase. At Re=200, the recirculation zone emanating from the aft of a cylinder in the array is extending to the front of the adjacent cylinder in the same column due to momentum gained by the fluid at increased inertia. The size of this recirculation bubble is growing in width, and a fair quantity of nanofluid is trapped inside this bubble, forcing the fluid to flow towards the adjacent cylinders. The interaction between the subsequent cylinders is maximum at Re=200 due to the appearance of the recirculation zone behind the cylinders. The streamlines are getting nearer to the surfaces of the cylinders at higher Re, and the lean boundary layer is forming on the surfaces of the cylinders.

The isotherms are getting denser around the surfaces of the three cylinders constituting the array on increasing Re, as depicted in Fig. 7, indicating the rise in the thermal gradients. At Re=10, the viscous forces are not negligible compared to inertial forces, and heat transfer is not entirely controlled by convection; rather, conduction also plays a part in contributing to the heat transfer. The thermal boundary layer is thicker at low Re, and its width decreases with an increase in Re, which ultimately causes higher heat transfer rates. When Re is increased, the crowding of isotherms in the proximity of the cylinders takes place (Fig. 7). The accumulation of isotherms near the surfaces of the cylinders at higher Re is due to the wake recirculation at the rear of the cylinders. It is also observed that the isotherms are clustered at the front of upstream cylinders. This can be due to the reality that the unheated bulk nanofluid first comes into the contact of upstream cylinders, which are at a higher temperature and result in steeper temperature gradients. For Re≥50, thermal plumes originate from the aft of the cylinders, and these thermal plumes are getting sharper at Re=100 and 200. The emergence of thermal plumes is momentum driven in the present situation as buoyancy has not been taken into account. Fig. 8 demonstrates the thermal patterns across the triangular array for different shapes of nanoparticles. The isotherms are getting denser near the surfaces of the cylinders when cylindrical or platelet-shaped particles are used, which indicates that thermal gradients are more near the surface when spherical nanoparticles are replaced with non-spherical ones and an increment in thermal gradient will eventually augment heat transfer from the cylinders. In the domain, the total surface area between fluid and solid interface changes on employing the different shapes of nanoparticles in a base fluid. The thermal conductivity of a nanofluid is directly proportional to the interfacial area [36]. It is known from the present calculations using Eq. (17) that platelet-shaped nanoparticles have

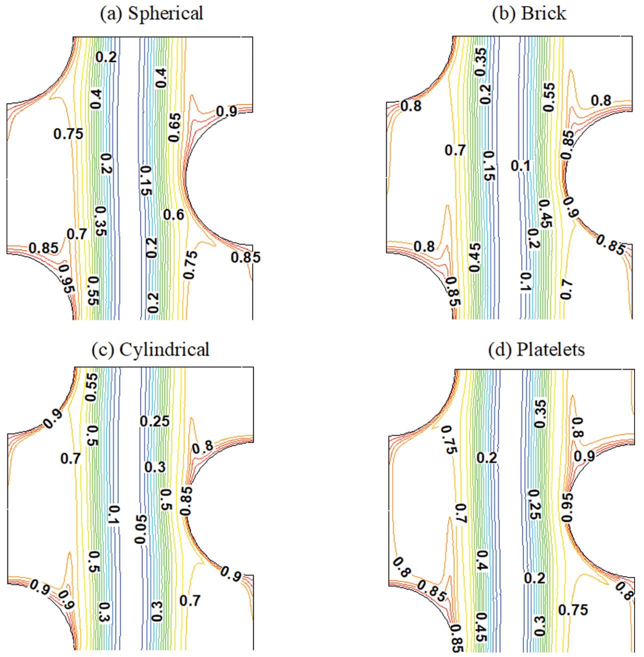

Fig. 8. Isotherms across an array of cylinders for different shapes of nanoparticles at Re=200.

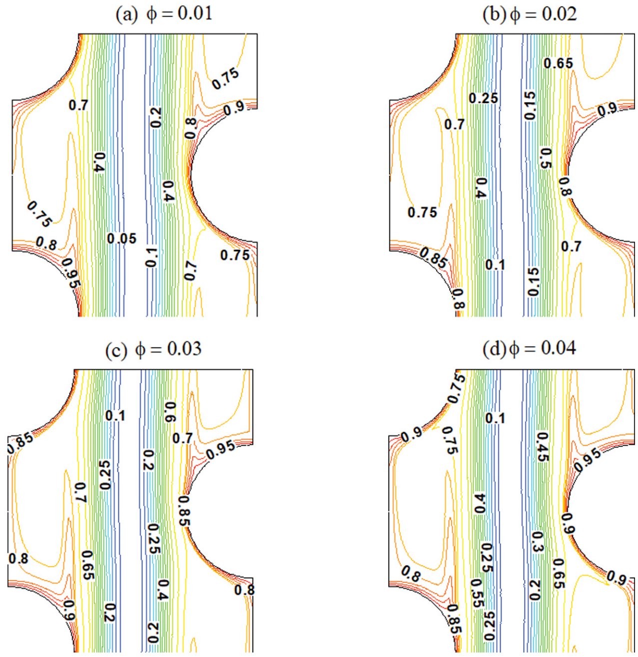

Fig. 9. Isotherms across an array for platelet-shaped nanoparticles at different volume fractions and fixed Re=200.

the highest thermal conductivity for a given nanoparticle concentration. So it can be said that the interfacial surface area is the highest for platelet-shaped nanoparticles employed in a nanofluid and which is also the cause of augmentation in thermal gradients when platelet-shaped particles are used in a base fluid. Hence it is augmenting the overall heat transfer.

Fig. 9 describes the aftermath of particle volume fraction, ϕ on the isotherms at Re=200 for platelet-shaped nanoparticles, followed by cylindrical and brick-shaped nanoparticles. For brevity, the effect of ϕ on thermal patterns across the triangular array of cylinders is shown only for platelet-shaped particles. It is observed that on increasing ϕ from 0.01 to 0.04, the isotherms are getting denser in the vicinity of cylinders. The thermal plumes are also getting sharper at higher concentrations of nanoparticles. These two observations resulted from an increment in the effective thermal conductivity of the nanofluid at higher values of ϕ and culminated in a surge in temperature gradients. The thermal boundary layer thinning is also taking place on increasing ϕ, which results in higher heat transfer rates.

Nanoparticle shape has a more profound impact on the velocity distribution across the array, as shown in Fig. 10. The velocity magnitude across the triangular array is significantly higher for cylindrical and platelet-shaped nanoparticles. Even the brick-shaped nanoparticles cause an increment in the velocity distribution across the array, although the increase is not at par with cylindrical and platelet-shaped nanoparticles. This increment in the velocity can

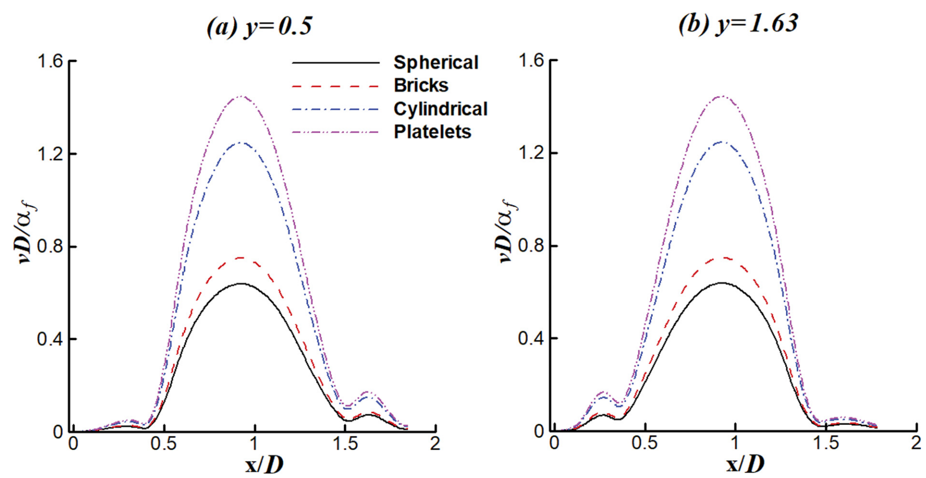

Fig. 10. Impact of nanoparticle shapes on velocity profile across periodic array at different locations.

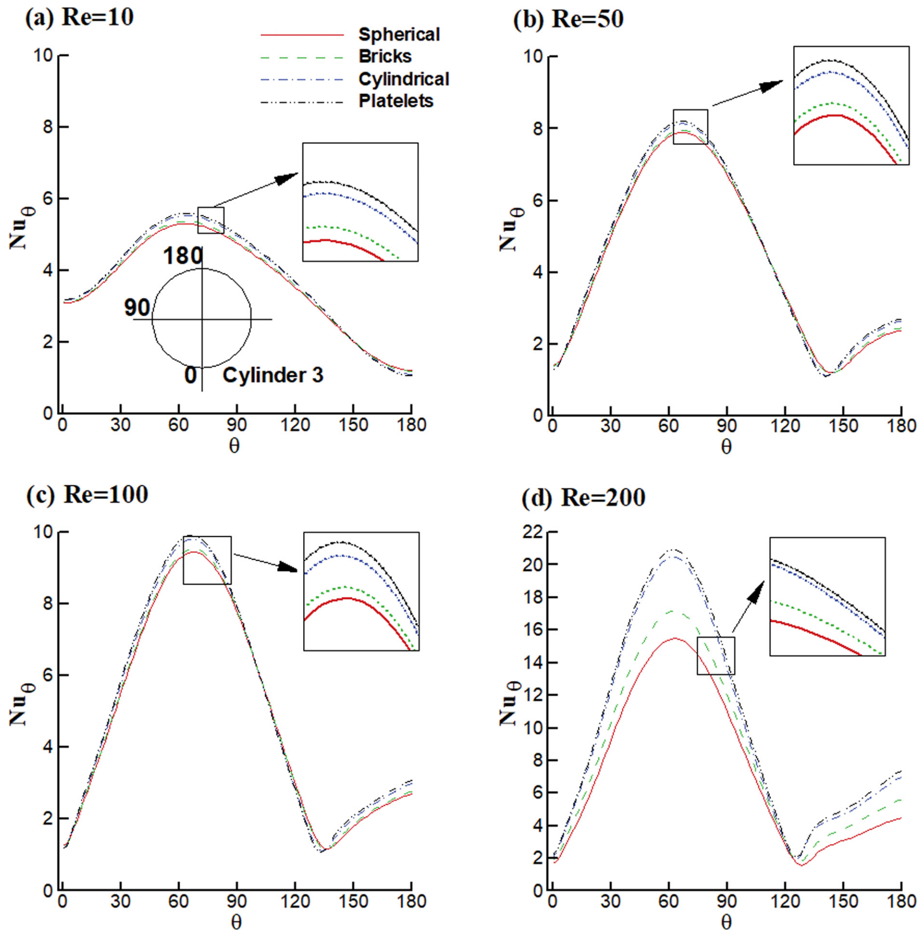

Fig. 11. Effect of nanoparticle shapes on local Nusselt number over cylinder 3 at ϕ=0.04 and different Re.

be ascribed to an increment in effective viscosity of nanofluids when non-spherical alumina nanoparticles are used for a fixed Re and nanoparticle volume fraction.

2. Nusselt Number

The impact of the shape of the alumina nanoparticle on the local Nusselt number Nu_θ around the surface of a cylinder in an equilateral triangular array is shown in Fig. 11. At Re=10, the variation in Nu_θ allocation on the surface of cylinder 3 with the shape of the nanoparticles is insignificant. On increasing Re, the difference in Nu_θ is getting noticeable with the shape of the nanoparticle (Fig. 11). At Re=200, the difference among Nu_θ for differently shaped nanoparticles is the highest. Platelet-shaped nanoparticles have greater values of Nu_θ, with cylindrical particles coming second. The distribution of Nu_θ on the cylinder surface for brick-shaped nanoparticles is also higher than the distribution of Nu_θ for spherical nanoparticles, although much lesser than platelet and cylindrically shaped nanoparticles (Fig. 11). The more elongated a particle is, the higher will be the heat transfer [36]. The local maxima for Nu_θ are not occurring at the frontal stagnation point (θ=0°) for all Re values; rather, it appears further away on the cylinder's surface because the fluid arriving at the front stagnation point is heated already by the preceding cylinder in the same column. The minimum value of Nu_θ is found at the separation point for all values of Re except Re=10 because no flow separation is taking place at Re=10 (Fig. 6). For Re>10, Nu_θ is increasing slightly up to the rear stagnation point (θ=180^0), as shown in Fig. 11, due to the emergence of the recirculation bubble behind the cylinder's surface (Fig. 6), which is continuously extracting heat from the heated cylinder. Fig. 12 depicts the alteration in the appropriation of Nu_θ on the surface of cylinder 3 with ϕ for distinct shapes of alumina nanoparticles. The highest values of Nu_θ appear at ϕ=0.04 for all shapes of nanoparticles. This is because the higher the ϕ, the higher will be the augmentation in the thermal conductivity of the nanofluid, which will eventually lead to a higher rate of heat transfer. The increment in Nu_θ values with ϕ is maximum for platelet-shaped nanoparticles.

Fig. 13 displays the change in mean Nusselt number Nu_m of the triangular array of circular pin-fins with ϕ, Re, and shape of the alumina nanoparticles. The highest Nu_m has appeared for platelet-shaped nanoparticles for all values of ϕ and Re and followed by cylindrical, brick, and spherical-shaped nanoparticles. The primary reason for high transfer rates in platelet-shaped particles followed by cylindrical and brick-shaped nanoparticles is their elongated structure compared to spherical particles [38]. At ϕ=0.04 and Re=200, the Nu_m is enhanced by 22% when spherical particles are replaced by platelet ones and by 17% when replaced by cylindrical ones. The enhancement in heat transfer is more considerable at higher Re. However, heat transfer enhancement is also taking place

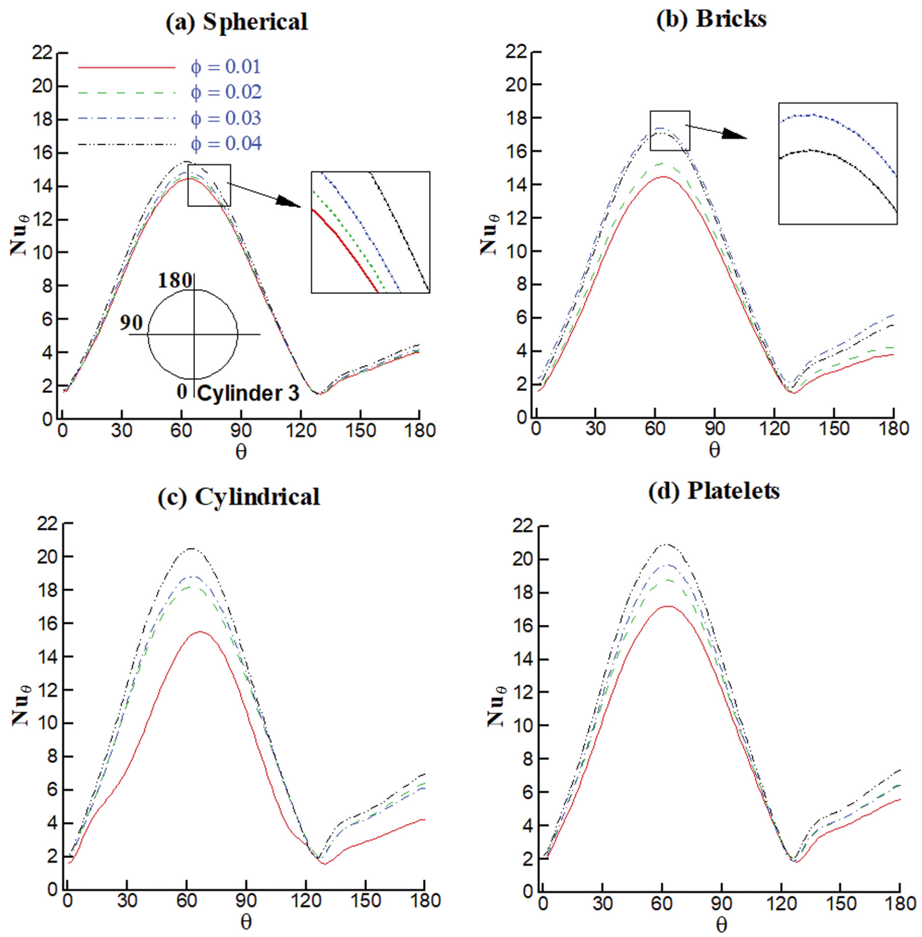

Fig. 12. Effect of particle concentration on local Nusselt number on cylinder 3 at Re=200 for different shapes. θ is the angle determined anti-clockwise from the aft of the cylinder.

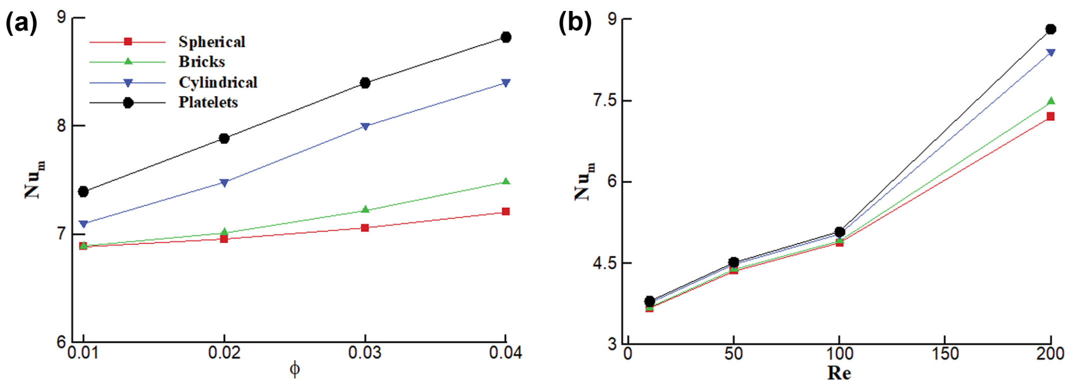

Fig. 13. Variation of mean Nusselt number of the array with nanoparticle shapes (a) at different ϕ and Re=200 and (b) at different Re and ϕ=0.04.

at lower Re (<200) when the spherical nanoparticles are replaced by other shapes, but the influence of shapes of nanoparticles on heat transfer is quite significant at Re=200.

The data obtained from the present study is used to develop mathematical correlations for Nu_m using regression analysis, and the following correlations are established for the four shapes of nanoparticles:

$$Nu_m=3.63[1+1.02\times10^{-03}\phi^{0.06}Re^{1.33}] \quad \text{(spherical)} \tag{22}$$

$$Nu_m=3.66[1+9.29\times10^{-04}\phi^{0.11}Re^{1.39}] \quad \text{(bricks)} \tag{23}$$

$$Nu_m=3.78[1+4.6\times10^{-04}\phi^{0.23}Re^{1.62}] \quad \text{(cylindrical)} \tag{24}$$

$$Nu_m=3.85[1+2.6\times10^{-04}\phi^{0.24}Re^{1.75}] \quad \text{(platelets)} \tag{25}$$

The coefficient of determination (R^2) for the above Eqs. (22)-(25)

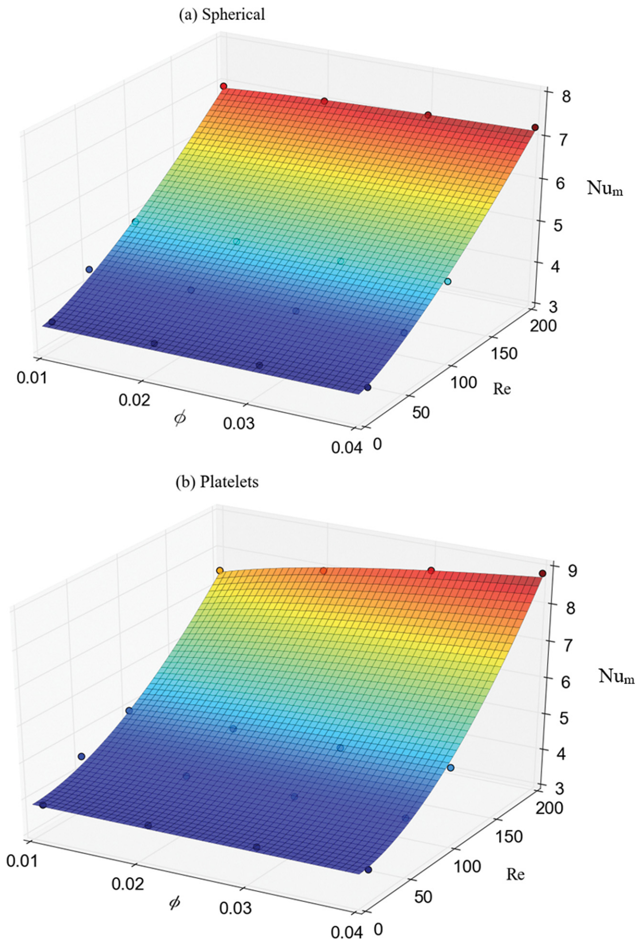

Fig. 14. Comparison between the present results and curves obtained from the correlations (Eqs. (22) and (25)).

is nearly close to 1, and the standard error is falling under 0.2, which proves the accuracy of these correlations. The comparison between the present computational results and correlation values is shown in Fig. 14. For the sake of brevity, the comparison for spherical and platelet-shaped nanoparticles is presented. More than 95% of the values obtained in the present study are lying on the curves obtained from the derived correlations, as depicted in Fig. 13.

3. Pressure Drop

The use of nanofluids certainly enhances heat transfer across heat exchange systems, such as the present one. However, it comes with an adverse effect of an increment in the effective viscosity, which subsequently results in relatively high pressure drops with respect to normal working fluids such as water, air, etc. Figs. 15(a) and 15(b) depict the variation in pressure drop with nanoparticle concentration and Re, respectively, for different shapes of nanoparticles. At the lowest nanoparticle concentration of ϕ=1%, there is a slight difference in pressure drop obtained for various shaped nanoparticles (Fig. 15(a)). The pressure drop across the heat exchange array is rising when the particle concentration is increased due to an increment in the suspension (effective) viscosity of the working fluid with the addition of nanoparticles. The increment in effective viscosity of the nanofluid is the highest for platelet-shaped nanoparticles, which results in a greater pressure drop compared to other shapes of nanoparticles such as cylindrical, bricks, and spherical for all values of particle concentration. The pressure drop is also increasing with Re, as shown in Fig. 15(b), which is a direct consequence of augmentation in the fluid velocity. Meanwhile, at a fixed Re, the pressure drop is the highest for platelet-shaped nanoparticles. It is noticeable from Fig. 8 that nanofluid having platelet-shaped alumina nanoparticles has the utmost velocity magnitude inside the array channel. On the other hand, nanofluid having spherical shaped nanoparticles has the lowermost pressure drop.

4. Pumping Power

Fig. 16 shows the change in pumping power (PP) required to pump the alumina nanofluid as a function of nanoparticle concentration and Re for different shapes of nanoparticles. Pumping power increases with an augmentation in nanofluid concentration for all shapes of nanoparticles (Fig. 16(a)). This is because the viscosity of the nanofluid increases with the surge in nanoparticle concentration; higher nanoparticle concentration in nanofluids causes fluid shear-thickening [39,40], which is the leading cause of augmentation in the effective viscosity of the nanofluids.

The pumping power also surges with proliferation in Re, as de-

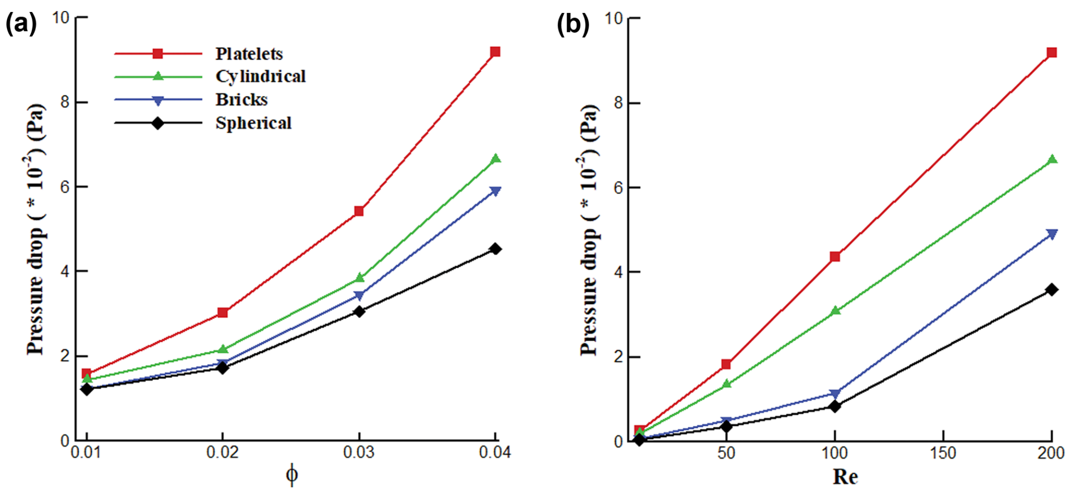

Fig. 15. Variation of the pressure drop with the volume fraction of nanofluid and Re for different nanoparticle shapes.

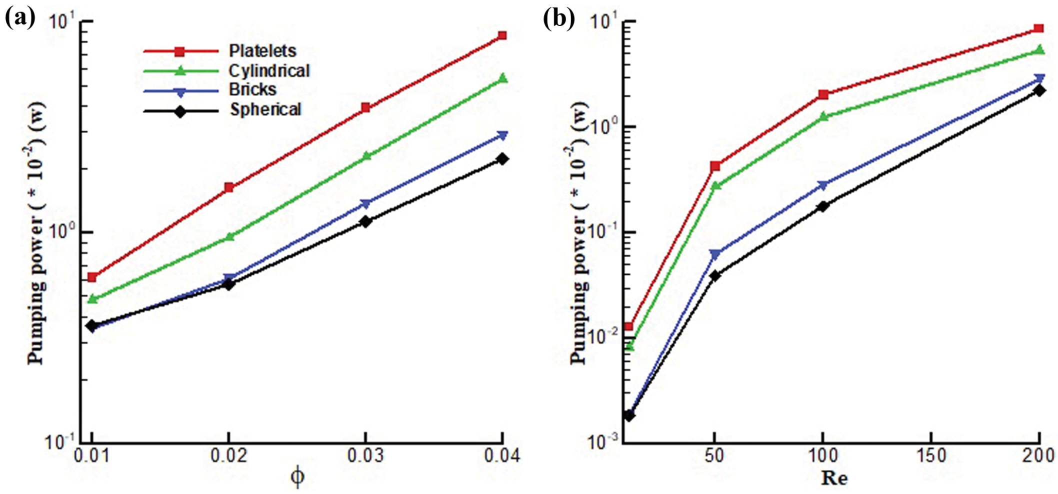

Fig. 16. Variation of the pumping power PP with the volume fraction of nanofluid and Re for different nanoparticle shapes.

picted in Fig. 16(b). The reason is an increment in the fluid velocity, which ultimately leads to greater pressure drop and higher pumping power required to pump the nanofluid. Pumping power is the highest when platelet-shaped particles are used due to the higher resultant viscosity of nanofluids, followed by cylindrical, brick, and spherical-shaped nanoparticles. The viscosity of nanofluid with non-spherical particles is greater in comparison to the nanofluid with spherical particles at any given concentration of nanoparticles. The rod-like structure of non-spherical nanoparticles and their elongated agglomerate hinders the Brownian motion of the particles for these rod-like elongated particles. Brownian motion includes both translation and rotational motion of the nanoparticles. This hindrance restricts the movement of nanofluids, causing an increment in the resultant viscosity of nanofluids, which in turn results in higher pumping power [36,38].

When the concentration of nanoparticles is low, the distance between the respective nanoparticles is larger than the longest nanoparticle; then, the rotational and translational motion of nanoparticles is not hindered by one another. Hence, the nanofluid will have low viscosity irrespective of the shape of the nanoparticle. For the higher concentration of nanofluids, the respective nanoparticles start colliding with each other. The rod-like nanoparticles form random clusters and agglomeration and elongate in such a way that limits both translational and rotational movements [36,38]. This restriction in normal flow causes an elevation in viscosity and pumping power needed to pump the nanofluid increases.

At the lowest values of nanoparticle concentration and Re (i.e., at ϕ=1% and Re=10), there is only a meager disparity between the pumping power for spherical and brick-shaped nanoparticles.

CONCLUSIONS

The present work comprehensively demonstrates the effect of alumina nanoparticle shape, nanoparticle concentration (0.01-0.04), and Reynolds number (10-200) on heat transfer from an equilateral triangular array of heated cylinders in a pin-fin type heat-exchanger. Comparing the heat transfer results obtained with different shapes of nanoparticles shows that platelet-shaped nanoparticles are best suited for higher heat transfer rates. The results demonstrate that using platelet-shaped alumina nanoparticles in place of spherical ones enhances the heat transfer across the triangular array of pin-fins up to 22% at Re=200 and ϕ=0.04, followed by cylindrical-shaped nanoparticles (up by 17%). For the platelet-shaped nanoparticles, streamwise local velocity has the highest value, causing higher heat transfer due to increased fluid inertia. Brick-shaped nanoparticles do not have a significant effect on heat transfer rates; replacing spherical-shaped particles with brick-shaped nanoparticles only enhanced heat transfer rates by 2% at Re=200 and ϕ= 0.04. Hence, brick-shaped nanoparticles are not the best for improving heat transfer rates. Besides, an unnecessary increase in the resultant viscosity of nanofluids makes them unsuitable for industrial use. The Re has a profound effect on heat transfer, which is evident due to increased fluid inertia and the momentum gained by the fluid at higher Re. The Nu_m augments by 137% for platelet-shaped nanoparticles when Re is increased from 10 to 200 at ϕ= 0.04. Similarly, for cylindrical nanoparticles, Nu_m augments by 120% when Re is increased from 10 to 200 at ϕ=0.04. An increase in nanoparticle volume fraction from 0.01 to 0.04 enhances the Nu_m by 23% for platelet-shaped nanoparticles at Re=200 and by 15% for cylindrical nanoparticles. It is recognized that pressure drop and pumping power increase with an increase in nanoparticle volume fraction and Re. Alumina-water nanofluid with platelet-shaped nanoparticles displayed the maximum pressure drop and pumping power due to the higher resultant viscosity of nanofluids when platelet-shaped nanoparticles were used.

NOMENCLATURE

C_P : coefficient of pressure
c_p : specific heat of the fluid [J/Kg·K]
D : cylinder diameter [m]
h : convective heat transfer coefficient [W/m^2·K]
k : thermal conductivity of fluid [W/m·K]
L : center to center distance between cylinders [m]

Nu_m : average Nusselt number
Nu_θ : local Nusselt number
Pr : Prandtl number
p : pressure [Pa]
$\hat{p}$: dimensionless pressure
r : radius of the cylinder [m]
Re : Reynolds number
$\hat{T}$: dimensionless temperature
T : free stream temperature [K]
U : volume averaged velocity [m/s]
u : cross stream velocity [m/s]
$\hat{u}$: dimensionless cross-stream velocity
v : stream-wise velocity [m/s]
$\hat{v}$: dimensionless stream-wise velocity
x, y : cartesian co-ordinates [m]
$\hat{x}$, $\hat{y}$: dimensionless cartesian co-ordinates
α_f : thermal diffusivity [m^2/s]
ϑ : kinematic viscosity [m^2/s]
ε : porosity of the array
μ : viscosity [Pa·s]
ρ : density [kg/m^3]
ψ : stream function
ϕ : nanoparticle volume fraction
θ : surface angle [degree]

Subscripts

w : wall
f : fluid
∞ : free stream
nf : nanofluid

REFERENCES

1. V. K. Mandhani, R. P. Chhabra and V. Eswaran, *Chem. Eng. Sci.*, **57**, 379 (2002).
2. A. Eidsath, R. G. Carbonell, S. Whitakar and L. R. Herrmann, *Chem. Eng. Sci.*, **38**, 1803 (1983).
3. A. R. Martin, C. Saltiel and W. Shyy, *Int. J. Heat Mass Transf.*, **41**, 2383 (1998).
4. C. Y. Wang, *Appl. Math. Model.*, **23**, 219 (1999).
5. W. Mughal, C. Xin, Y. Zhang, I. Samo, M. Abro and Y. He, *Chem. Eng. Res. Des.*, **151**, 231 (2019).
6. C. A. Rubio-Jimenez, S. G. Kandlikar and A. Hernandez-Guerrero, *IEEE Trans. Components, Packag. Manuf. Technol.*, **2**, 825 (2012).
7. S. Ndao, Y. Peles and M. K. Jensen, *Int. J. Heat Mass Transf.*, **70**, 856 (2014).
8. A. K. Saha and S. Chanda, *Int. J. Therm. Sci.*, **137**, 325 (2019).
9. C. T. Nguyen, G. Roy, C. Gauthier and N. Galanis, *Appl. Therm. Eng.*, **27**, 1501 (2007).
10. R. P. Ram, R. P. Bharti and A. K. Dhiman, *Can. J. Chem. Eng.*, **94**, 1381 (2016).
11. M. Asif and A. Dhiman, *J. Brazilian Soc. Mech. Sci. Eng.*, **40**, 1 (2018).
12. T. S. Wung and C. J. Chen, *J. Heat Transfer*, **111**, 633 (1989).
13. C. J. Chen and T. S. Wung, *J. Heat Transfer*, **111**, 641 (1989).
14. A. Žkauskas, *Adv. Heat Transf.*, **18**, 87 (1987).
15. T. R. Vijaybabu, *Int. J. Mech. Sci.*, **166**, 105240 (2019).
16. M. Sheikholeslami, R. ul Haq, A. Shafee, Z. Li, Y. G. Elaraki and I. Tlili, *Int. J. Heat Mass Transf.*, **135**, 470 (2019).
17. A. H. Pordanjani, S. Aghakhani, M. Afrand, B. Mahmoudi, O. Mahian and S. Wongwises, *Energy Convers. Manag.*, **198**, 111886 (2019).
18. M. Sheikholeslami and M. K. Sadoughi, *Int. J. Heat Mass Transf.*, **116**, 909 (2018).
19. M. Sheikholeslami, *Phys. Lett. Sect. A Gen. At. Solid State Phys.*, **381**, 494 (2017).
20. S. A. Mikhailenko, M. A. Sheremet, H. F. Oztop and N. Abu-Hamdeh, *Int. J. Mech. Sci.*, **156**, 137 (2019).
21. F. Selimefendigil and H. F. Öztop, *Int. J. Mech. Sci.*, **157**, 726 (2019).
22. A. Bouzerzour, M. Djezzar, H. F. Oztop, T. Tayebi and N. Abu-Hamdeh, *Phys. A Stat. Mech. its Appl.*, **538**, 122479 (2019).
23. M. Asif, R. Chaturvedi and A. Dhiman, *J. Therm Sci. Eng. Appl.*, **13**, 041025 (2021).
24. M. Sheikholeslami and S. A. Farshad, *Powder Technol.*, ***378***, 145 (2021).
25. R. D. Selvakumar and S. Dhinakaran, *Int. J. Heat Mass Transf.*, **106**, 816 (2017).
26. A. M. Lavasani and H. Bayat, *Energy Convers. Manag.*, **129**, 319 (2016).
27. H. C. Brinkman, *J. Chem. Phys.*, **20**, 571 (1952).
28. J. C. Maxwell, *A treatise on electricity and magnetism*, Oxford, England (1873).
29. T. K. Nguyen, A. Saidizad, M. Jafaryar, M. Sheikholeslami, M. B. Gerdroodbary, R. Moradi, A. Shafee and Z. Li, *Chem. Eng. Res. Des.*, **146**, 478 (2019).
30. R. Ellahi, M. Hassan and A. Zeeshan, *Int. J. Heat Mass Transf.*, **81**, 449 (2015).
31. S. M. Vanaki, H. A. Mohammed, A. Abdollahi and M. A. Wahid, *J. Mol. Liq.*, **196**, 32 (2014).
32. R. Pravesh, A. Dhiman and R. P. Bharti, *Int. J. Heat Mass Transf.*, **130**, 1141 (2019).
33. C. K. Mangrulkar, A. S. Dhoble, S. Chamoli, A. Gupta and V. B. Gawande, *Renew. Sustain. Energy Rev.*, **113**, 109220 (2019).
34. J. Buongiorno, *J. Heat Transfer*, **128**, 240 (2006).
35. M. Corcione, *Energy Convers. Manag.*, **52**, 789 (2011).
36. E. V. Timofeeva, J. L. Routbort and D. Singh, *J. Appl. Phys.*, **106**, 014304 (2009).
37. C. F. Lange, F. Durst and M. Breuer, *Int. J. Heat Mass Transf.*, **41**, 3409 (1998).
38. N. C. Maji and J. Chakraborty, *Int. J. Heat Mass Transf.*, **156**, 119709 (2020).
39. T. Ambreen, A. Saleem and C. W. Park, *Appl. Therm. Eng.*, **158**, 113781 (2019).
40. S. M. S. Murshed and P. Estellé, *Renew. Sust. Energy Rev.*, **76**, 1134 (2017).